

# Microstructures and Formation of Tundish Clogging Deposits in Ti-Alloyed Al-Killed Steel



ENNO ZINNGREBE, JAMES SMALL, SIEGER VAN DER LAAN,  
and ALBERT WESTENDORP

The continuous casting of Ti-alloyed Al-killed steels traditionally experiences clogging in the tundish, impeding stable operation. We studied the microstructures and mode of formation of such clogging deposits in tundish skulls recovered after long cast series. We sampled the steel skull along the whole tundish bottom from under the ladle shroud (impact zone) up to the tundish well and nozzle. The microstructures imply that the steel solidifies to the refractory (gunning mass) and remains partially solid through the entire cast. Thus, a “mushy zone” of steel loaded with solid delta ferrites is present along the margins of the steel during casting. In this mushy zone, the widely observed clusters of variably sintered alumina (NMI) accumulate, along with a substantial amount of gas bubbles acting as inclusion scavengers. The clustered alumina particles show a lognormal particle size distribution (PSD) in all locations, which becomes more pronounced if correcting for the observable sintering. Sintering of alumina size distributions linearizes a PSD, and further evolution, once the deposit is locked in place, occurs by Ostwald ripening, introducing skewness to the distributions. The observed PSDs contrast with the established log-linearity of PSDs of individual floating alumina NMI in the bulk steel, and suggest that the source of the alumina in the clogging deposits is not the passing bulk steel. However, ubiquitous sedimentary features show that the alumina particles are also not grown by reoxidation *in situ*. An upstream source separate from the bulk stream must be inferred, which is also required by the consistent sporadic presence of oxidic materials which cannot be derived from local sidewall reaction. In summary, the development of clogging deposits in this type of steel is an example of “slurry casting” of partially solidifying steel over thermal loss surfaces of refractories in the nozzle area.

<https://doi.org/10.1007/s11663-020-01903-y>

© The Minerals, Metals & Materials Society and ASM International 2020

## I. INTRODUCTION

ONE of the longstanding problems in the production of steels is the occurrence of clogging of the continuous casting installations during casting of liquid steel. In aluminum killed steels, the clogging most often consists of alumina ( $\text{Al}_2\text{O}_3$ ) accumulations found at various locations in the continuous casters, most notably in the ladle shroud, the tundish well, and/or the submerged entry nozzles or shrouds.<sup>[1–5]</sup> The fundamental mechanisms, to which the formation of inclusion accumulations are generally attributed, fall into two main groups. Since the steel is strongly non-wetting to most oxide surfaces, it is often assumed that pre-existing particles

floating in the steel liquid stick to refractory. This type of mechanism is “depositional”, meaning the particles are not formed at the clog location (*e.g.*, Refs. 2, 6 through 8). A second mechanism involves reoxidizing steel sidewall reactions, in which oxygen is locally added to the steel (from gases such as CO or ambient air, or from reducible oxides in the refractory). This oxygen then precipitates new alumina particles by recombining with the dissolved aluminum in the steel, creating a clog *in situ*. This mechanism is independent of the amount of previously existing particles in the steel melt (such as alumina from deoxidation) (*e.g.*, Refs. 3, 4, 9 through 12). Both mechanisms can also be combined in the generation of a particular clog. However, there is a lack of studies that demonstrate the actual operation of either mechanism from observations of the real casting process.

It is well known that Ti-alloyed Al-killed steels are especially sensitive to clogging (*e.g.*, Ref. 13). It is not generally permissible to assume that the mechanisms leading to clog formation are the same in the different parts of the caster system. Specifically, it has to be expected that mechanisms of clog formation at ladle

---

ENNO ZINNGREBE, JAMES SMALL, SIEGER VAN DER LAAN, and ALBERT WESTENDORP are with Tata Steel, R&D, P.O. Box 10000, 1970 CA IJmuiden, The Netherlands. Contact e-mail: [Enno.Zinngrebe@tatasteelleurope.com](mailto:Enno.Zinngrebe@tatasteelleurope.com)

Manuscript submitted July 31, 2018.

This article was updated to correct image citation and ordering errors introduced during production.

Article published online July 23, 2020.

**Table I. Typical Composition of the Ti-Alloyed Al-Killed Steel Casts**

Element	C	N	S	Al	Si	Ti	Mn
ppm	15 to 20	20	70	200 to 400	30 to 50	400 to 500	1100

well/gate (including well filler sand); at tundish bottom and well; and in the SEN respectively are qualitatively different phenomena. Most published research on clogging deals with clogging in the SEN. From an operational standpoint however, a clogged SEN can be changed without significant interruption of the casting series. Clogging in the tundish terminates a casting series, and therefore has a larger operational effect, but is far less studied in the literature because of the difficulty of obtaining post-mortem samples. The tundish well is also where Ti-alloyed Al-killed steels tend to build-up a growing clog over many heats, limiting casting series lengths.<sup>[13]</sup> Therefore a research program has been carried out at Tata Steel Europe, IJmuiden steelworks, to investigate the mechanisms of formation of clogging of Ti-alloyed steel in the tundish.

## II. SAMPLES AND METHODS

The physical sampling of clogging deposits from post-mortem tundish skulls concentrated on casts of a specific grade of ultra-low carbon IF steel with moderate amounts of Ti and Al additions (Table I). For this steel grade, tundish skulls were obtained from long-series casts under both routine and test industrial practices, by ending the cast with significant amount of steel in the tundish and overturning it to drop the skull after solidification. The 70-ton straight-shaped tundish at Tata Steel IJmuiden Works has steel entry through a ladle shroud in the center, and two tundish wells feeding two casting strands close to the ends. Under the ladle shroud, an impact zone is present using thickened refractory, but no turbostop. When ladles are opened, their chromite-silica based well filler sand drops into the tundish at this location. Tundish wells (Figure 1) are shaped by well blocks made from an alumina-spinel castable, into which conical, porous nozzle stones are mounted, through which Ar is injected into the tundish nozzle bore. These well nozzles lead to a sliding gate flow control system. Refractory mortars are used between nozzle, well block, and surrounding tundish brickwork. In preparation of a cast, the inside surface of the tundish is gunned with a wet gunning mass (periclase-forsterite based). The tundish gunning mass is preheated, to remove residual water. During casting, the tundish is covered by an artificial calcium aluminate cover slag.

From the tundish skulls, steel blocks containing the steel/sidewall interfaces were cut at three positions: the tundish well itself, a tundish bottom location halfway between ladle shroud and tundish well, and directly under the ladle shroud (impact zone). From the recovered steel blocks, small sections of the interface were cut and prepared as polished mounts (2 to 6 cm size) for

microstructural investigations. In this study, microstructures of one sample each will be shown for the locations under ladle shroud and in the middle of the tundish bottom, and three samples will be shown from the tundish well, covering the inlet, slope, and vertical part of the tundish outlet. Optical microscopy was performed on all mounts using petrographic reflected light microscopes (Zeiss Axioplan and Z1 Imager) including optical particle measurements by image analysis (Zeiss AxioVision 4.8 software). SEM EDS analysis of the samples was done using W-filament as well as FEG equipped microscopes (Jeol 5900LV, Zeiss Ultra 55 and Jeol 7100F). Analysis conditions were 5 to 15 kV depending on material and beam currents around 1.5 to 3 nA. A Thermo Fisher Scientific Noran System Seven analysis system was used for quantifications. EPMA for minor elements was performed at Tata Steel IJmuiden on a 5-spectrometer Cameca SX-100, using a high beam current (300 to 800 nA at 15 kV) and long counting times (60 to 200 seconds) to achieve low detection limits. Accuracy of the analyses was checked against NIST steel standards 1763 and 1767 and found to be within 10 pct relative at the 40 ppm level. Descriptions of materials and phases throughout this work use the ceramic oxide notation (e. g. C, A, M, S as shorthand for the CaO, Al<sub>2</sub>O<sub>3</sub>, MgO, and SiO<sub>2</sub> as oxide compounds).

### A. Population Density Functions

In this paper, particle sizes of non-metallic inclusions are analyzed using the population density function methodology introduced by References 14 and 15. This methodology is based on measurement of sufficiently large particulate datasets (hundreds to thousands of particles per dataset) from images to allow treatment by population statistical methods. Simple histograms of frequency  $f(r)$  vs radius  $r$ , or descriptive numbers have the disadvantage that their numerical values are dependent on arbitrarily chosen settings such as bin width, bin distribution, sizes of observational areas. Population density functions (PDF) are designed to overcome these arbitrary choices and are defined as the change of particle frequency  $f$  as a function of size (diameter  $d$  or radius  $r$ ):

$$\text{PDF} = \frac{df}{dr}$$

PDF's are the preferred way of characterization of particle distributions in particulate engineering.<sup>[16]</sup> For the particle distributions in this work, a full stereological conversion from cross sectional data to three-dimensional distributions is used. This stereological conversion uses the CSDCorrections applet of Higgins,<sup>[17]</sup>

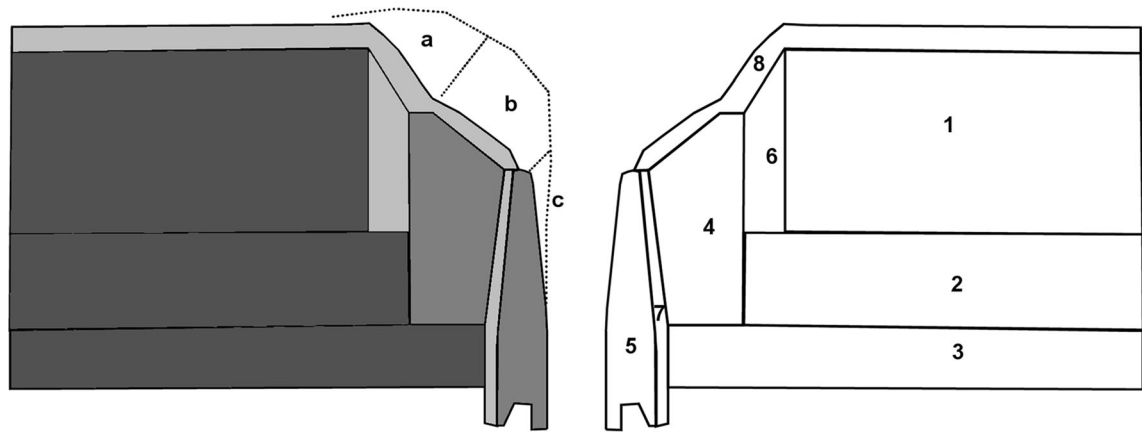


Fig. 1—Sketch of the construction of the tundish well in the sampled caster's tundish. Construction is centrosymmetric; refractory design elements are labeled by number in the right half. Tundish body elements are dark gray shaded, consumable shaped castable stones are mid gray, and unshaped masses and mortars are light gray shaded in left half. 1—sacrificial brickwork; 2—perennial brickwork; 3—outer body; 4—well block, 5—porous nozzle stone, 6 and 7—mortars, 8—tundish spray gunning mass. The occurrence of clogging materials in the tundish well is outlined by dotted line in the left half, subdivided into three structurally different zones: a—tundish floor to well inlet, b—main clogging buildup, c—clogging in the vertical flow zone, nozzle inlet.

obtainable from <http://www.uqac.ca/mhiggins/csdcorrections.html>, and follows methods described in References 14 and 15. All calculations use the equivalent circular particle diameter from measured particle areas (*i.e.*, neglecting particle shape) and assume three-dimensional isotropy of distribution. The obtained size distributions are plotted on double-logarithmical  $\ln \text{PDF}$  vs  $\log(r)$  or  $\log(d)$  diagrams. Recent work on the particle size distributions of alumina particles in Al-killed steel<sup>[14,15,18–22]</sup> has shown that the observed distributions reflect the physical processes operating in the steel melt. Active net transfer reactions leading to active nucleation and growth of new particles from elements dissolved in the steel melt leads to lognormal particle size distributions (curved on PDF plots), following the form<sup>[14,15,18]</sup>:

$$\text{PDF} = (c_0/d) \exp(-(\ln d - a)^2 / 2b^2) / \sqrt{2\pi b^2},$$

where  $d = 2r$  is the particle equivalent diameter,  $c_0$  is a scale factor, and the functional parameters  $a$  and  $b$  set maximum frequency size (peak), and wideness or sharpness of the distribution, respectively. Once active net transfer of material out of solution to growing particles stops (*i.e.*, at chemical equilibrium), physical collision-breakup processes between the particles, whose amount remains constant, turn such lognormal size distributions into power-law distributions that are linear on a double-log PDF plot. The collision-breakup equilibrium is determined by the physical force balances between interparticle and shear forces in the steel melt (modeled in Ref. 23, and observed in liquid steel in above cited works). The transformation of nucleation-growth controlled lognormal distribution into such log-linear power-law distributions is called linearization, and occurs within steel melts within minutes after desoxidation, see References 14, 18, and 21. After this linearization, typical as-cast Al-killed steel has a log-linear size distribution that is similar enough between different studies to warrant the definition of a “reference line”<sup>[14,18]</sup> of the form

$$\text{PDF} = a * r^{-b},$$

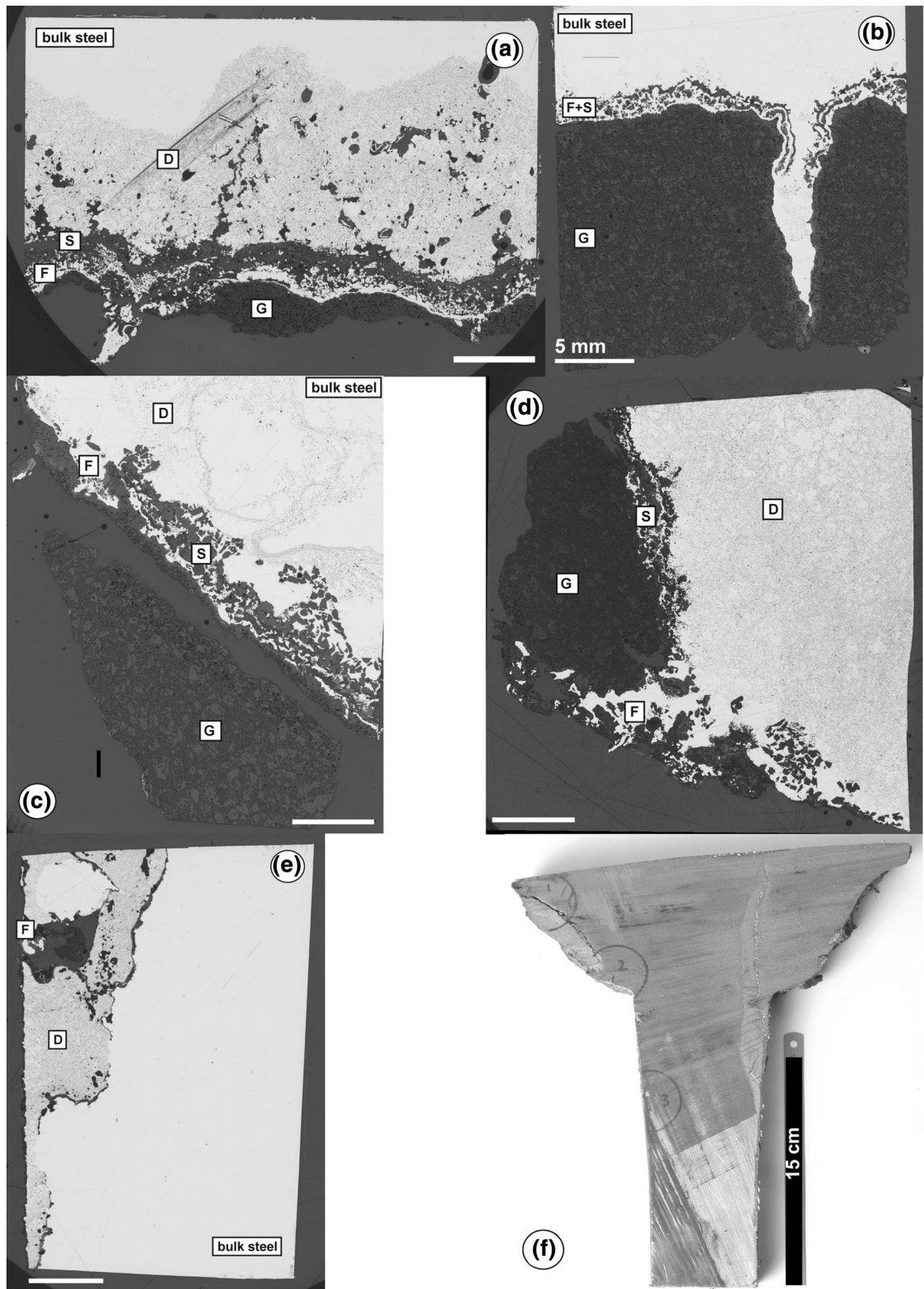
where the exponent  $b$  is the slope of the reference line, initially found as  $-3.5$  by Reference 14, but is possibly variable.<sup>[19,20]</sup> This would be the expected size distribution of alumina NMI floating in liquid steel and available during casting to collect into a clogging deposit. Thus, based on this work on floating NMI, size distributions of alumina particles in clogging deposits can be meaningfully interpreted in terms of their possible origins and processes shaping them.

### III. MICROSTRUCTURES OF THE CLOGGING DEPOSITS

In this section, a short overview of the microstructures along the steel-refractory interface encountered in the tundish is given, including clogging materials where present. The interface between steel skull and its adjoining refractories shows a recurring succession of microstructural zones which is found in every investigated skull. A characteristic example of the structural sequence is given in Figure 2, which shows microscopic images of polished mounts from a single tundish skull sampled at the five locations mentioned above. In general, at each location, a succession of five microstructural layers is found to make up the transition from sidewall into the steel skull body. These are:

1. The sidewall refractory itself, which is gunning mass along the whole length of tundish bottom and tundish well followed by the shaped piece of the tundish well nozzle stone. This microstructural zone is marked “G” on Figure 2 overview images.
2. A thin layer of continuous steel or disjointed pieces of steel that follows the details of the underlying interface topography but is devoid of included NMI such as alumina. This layer includes steel intrusions into





◀ Fig. 2—Overview images of the microstructures encountered at the steel-refractory interface along the tundish bottom. Each microscopic image is a reflected light image mosaic, with the white scale bar representing 5 mm. On the microscopic images, recurring microstructural elements are marked as: G = gunning mass, F = inclusion free steel at the refractory contact, S = “slag-like” heterogeneous oxide compound layers along the bottom, D = clogging material rich in alumina particles embedded in steel; and the bulk steel. Figure parts: (a) interface directly under the ladle shroud (impingement point). (b) Interface halfway between ladle shroud and tundish well. (c) Interface in the entrance section of the tundish well (a in Fig. 1). (d) Interface in the main clogging region of the tundish well (b in Fig. 1). (e) Interface in the nozzle itself, with the Ar-purging porous tundish nozzle stone at the left edge of sample. (f) Rough cut of the steel skull section through the tundish well before polished mounts were cut, with positions of the last three samples indicated.

gaps in the substrate, such as fractures within the gunning mass from the drying process. Such drying cracks appear as steel filled wedges in cross section (see Figure 2(b); also visible in deformed state in Figures 2(a) and (d)). This microstructural zone is marked “F” in Figure 2.

3. A band of disjointed fragments, or multiple layers of oxidic (“slag-like”) materials. These are very heterogeneous in makeup, and can contain relicts of well filler sand (such as in samples from under the ladle shroud, but found even in the tundish well), or other compositions whose common characteristic is that they can not be derived from refractory materials of the tundish (gunning mass, lining refractory or cover slag), and therefore must have been deposited from an upstream source. This band of displaced materials most often is found only on the bottom of

the tundish itself, not in the vertical flow section of the tundish nozzle. This microstructural zone is marked “S” in Figure 2.

4. A zone of steel rich in non-metallic inclusions, overwhelmingly of alumina, but also with a small content of  $MgAl_2O_4$  spinel and rarely other oxides. The volume percentage of oxide particles (quantified by optical image analysis) varies between ~ 2 and up to 10 vol pct but most often is around 5 to 7 vol pct. This particle rich but otherwise massive steel zone is also rich in microbubbles, voids of 10 to 1000  $\mu m$  diameter that can be occurring alone, or with particle-encrusted surfaces, or as trace outlines around a steel infilling (interpreted as bubbles that have collapsed during cooling). This steel-NMI zone is the material that is commonly understood to make up the clogging “deposits” in tundish wells, and it is best developed in the tundish wells, but we have observed it to occur irregularly along the tundish bottom, and regularly directly under the ladle shroud as well. This microstructural element is marked “D” in Figure 2.
5. The bulk steel itself. Although slowly solidified in the tundish after end of casting, it has the composition of the nominal bulk steel, and is characterized by sparse, disseminated single oxidic NMI, relatively large solidification TiN precipitates and can carry occasional alumina NMI clusters or cluster fragments close to the refractory sidewall. In the following, a more detailed description of the sample set from the exemplary skull shown in Figure 2 is given, according to the different sample locations along the tundish bottom. The microstructures are described together with an assessment of their significance.

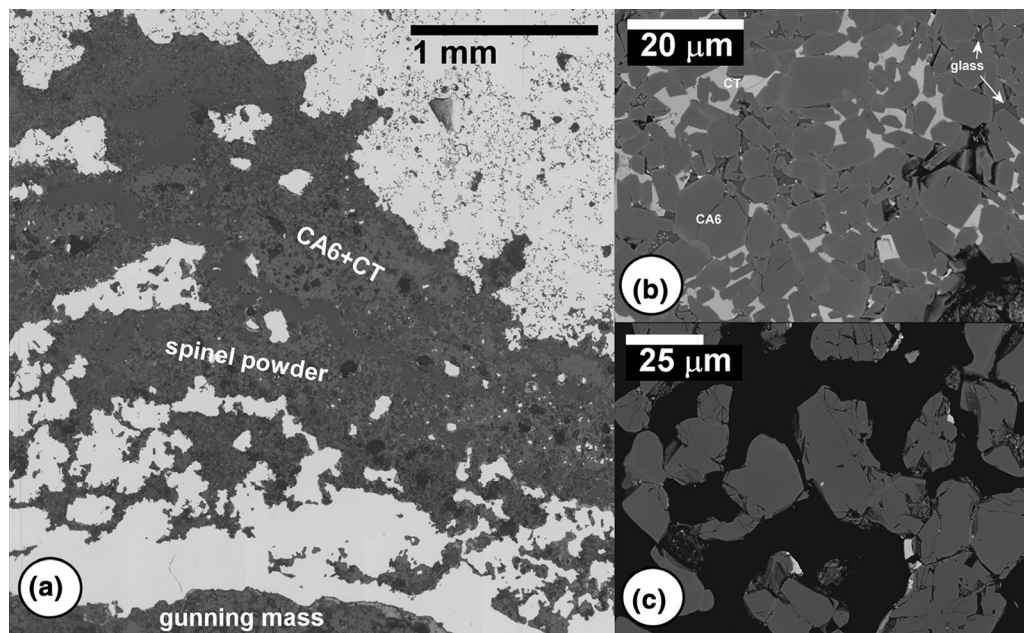


Fig. 3—Microstructures at the steel-gunning mass interface in Location A. (a) Enlargement of the contact area from Fig. 2 (reflected light image). (b) and (c) SEM BSE detail images of the CA6 + CT and spinel layers indicated in (a).

**Table II. Spot Analysis Data for Oxide Materials in Fig. 3**

Oxide	Na <sub>2</sub> O	MgO	Al <sub>2</sub> O <sub>3</sub>	SiO <sub>2</sub>	ZrO <sub>2</sub>	K <sub>2</sub> O	CaO	TiO <sub>2</sub> *	MnO*	FeO*	Phase ID
Image (b)											
1	0	1.8	77.0	0	0	0	7.4	8.2	1.1	3.9	CA6 core
2	1.0	1.3	67.7	0.5	0.2	0	5.5	14.5	1.1	7.6	CA6 rim
3	0.7	0	0.4	0.1	0.2	0	36.7	58.8	0.2	1.7	perovskite
4	8.9	0.1	40.0	41.4	0	3.2	1.4	3.4	0	0.9	glass
Image (c)											
1	0	26.83	63.90	0	0	0	0.01	4.32	0.79	3.99	spinel n = 7
2	0	0.18	0.26	0	0	0	0.01	0.17	0.05	0.48	σ
3	0	0.979	1.843	0	0	0	0	0.080	0.016	0.082	3 cations

\*Oxide quantified in this form irrespective of true valency.

*A. Microstructures at the Mid-tundish Bottom, Under Ladle Shroud*

This location was sampled in several Ti-alloyed cast skulls, as well as one skull from a non-Ti alloyed Al-killed cast. To our knowledge, no post-mortem descriptions of this location exist in published literature. Fresh liquid steel from the ladle here enters the tundish, subject to the turbulence of the ladle shroud passage but not yet changed by chemical interaction with refractory or tundish slag.

*1. Gunning mass interface and layers of oxidic material*

Figure 2(a) shows a microscopic overview image of an interface sample from this location. The interface is characterized by the development of a 1 to 2 cm thick zone of inclusion and bubble rich steel (D), atop a mixed layer of inclusion free steel with bands of oxidic materials (F, S) atop the original periclase to forsterite gunning mass (G). This configuration has been observed in all Ti-alloyed casts, but in the non-Ti alloyed cast, the thick inclusion rich zone (D) was largely absent. The top of the gunning mass has sintered into a coherent layer at the interface, with monticellite and merwinite constituting an intergranular ceramic bond. This coherent layer is no thicker than 100 to 200 μm (one to two refractory aggregate grain sizes). At larger distance from the steel, the gunning mass has not densified and displays a very open granular structure with about 30 vol pct porosity. Except in places where cracks allowed air access during cooling, no development of a FeO enrichment in the gunning mass periclase or of FeO<sub>x</sub> scale on steel is seen. The steel side of the interface shows an irregular mix of clean steel with oxidic materials (zone S), in which relicts of a more or less disrupted layering can still be seen. Whereas in non-Ti alloyed casts, the oxidic material often is clearly derived from ladle well filler sand as evidenced by occurrence of chromite, in the Ti-alloyed casts such as that shown in Figure 2, the oxidic layers consist of calcic and Ti rich phases not derived from well filler sand. Figure 3 shows an overview of its microstructures. The most characteristic assemblage is a packed accumulation of CA6 crystals, with intergranular CT (perovskite) cementing them together (Figure 3(b)). In this cumulate, the CA6 phase has a significant content of Ti<sup>3+</sup>, substituting for Al<sup>3+</sup>. The Ti content is increasing

towards the rim of individual crystals, overgrowing them as sharp Ti rich zones, where the Ti content ranges up to > 13 wt pct Ti<sub>2</sub>O<sub>3</sub>. In these rim zones, Na also enters the structure; Mg contents are low (< 2 wt pct MgO). The perovskite is largely pure CaTiO<sub>3</sub>. Besides the crystalline phases, there is a small amount of an intergranular glass, which has an alkaline aluminosilicate character (8 to 9 wt pct Na<sub>2</sub>O, 3 to 4 wt pct K<sub>2</sub>O, < 0.4 wt pct MgO, but no FeO content). Next to such titanate enriched materials, a loose powder of spinel appears in pockets in the steel (Figure 3(c)). This spinel is highly magnesian, but not aluminous: its octahedral site is completely filled with Mg, whereas roughly 8 mol pct of ulvospinel (MgFeTiO<sub>4</sub>) substitute on the tetrahedral site. Table II gives spot analysis data for these phases.

*2. Inclusion rich steel: NMI and microbubble microstructures*

The most significant microstructure of the impact zone sidewall is a mm to cm thick layer of inclusion rich steel (Figure 2, zone D). Figure 3 shows that this layer begins only atop the oxide bands (S); the steel foils (F) interlayered with the oxide bands are free of such inclusions. In the inclusion rich steel, the particles are overwhelmingly alumina NMI. Microstructures at bottom, middle and top of the inclusion rich steel differ slightly as illustrated in Figure 4. Compositionally, distinct subgroups can be recognized based on the Ti content of the inclusions: some NMI have TiO<sub>2</sub> below detection limit of the EDS (ca. 0.1 wt pct TiO<sub>2</sub>); others have a TiO<sub>2</sub> content of 0.8 to 1.5 wt pct. A third group with high Ti content has internal micron to sub-micron sized inclusions of steel, TiN, aluminotitanates or voids and is relatively large (typically about 10 to 15 μm diameter) and subspherical. These alumina particles are believed to be relicts from Ti alloying during ladle refining (see description in Ref. 14; an example is shown in Figure 4(e)). The volume fraction of inclusions decreases gradually from 11 vol pct at the bottom to 7 vol pct at the top of the inclusion rich zone (towards the bulk steel). Next to inclusions, the zone also is rich in microbubbles with diameters between several 10 seconds to several hundreds of μm. The volume percentage of bubbles varies widely in no apparent systematic order with depth in the clog. Such bubbles can be found with



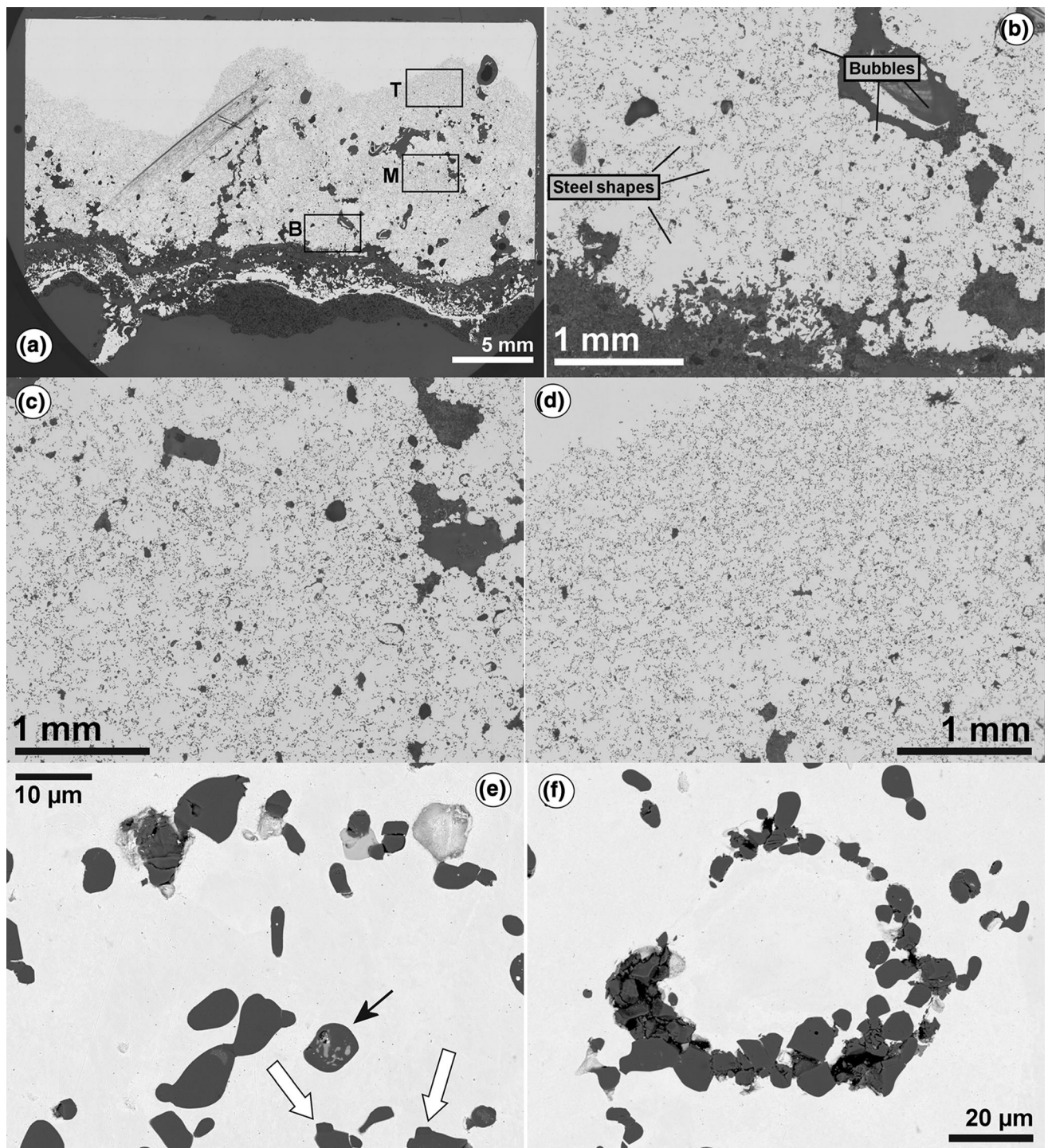


Fig. 4—Microstructures of the inclusion rich zone in the impact zone skull sample. (a) Full sample overview (same as in Fig. 2), on which three areas are marked across the inclusion rich zone whose microstructures have been quantified: Bottom (B), Top, Middle (M), and Top (T). The three areas are enlarged in the three clockwise following panels ( $\times 200$  magnification optical base images, (b, c, d). (e) and (f) are SEM BSE images of peculiar inclusion structures: (e) shows alumina with Ti, Zr rich sub-inclusions (black arrow) and spinels atop alumina (white arrows—angular grains) and (f) shows a bubble encrustation ring of alumina particles around an “infilled” bubble.

clean surfaces to steel, but most often they have surfaces that are encrusted with alumina NMI. Many inclusion clusters trace perfectly round shapes, and are interpreted as infilled bubbles (see Figure 4(f) for a well-preserved example). Moreover, many crescent-shaped and

half-rounded aggregations of alumina can be found in this zone that may be relicts of original bubbles in which the bubble encrustation has broken up. Thus, a significant fraction of inclusions in the zone may have gone through a bubble capture stage. Image analysis counting

**Table III. Observational Data for Clogging Particle Size Measurements at a Tundish Impact Pad**

Image	Substrate Distance (mm)	Obs. Area (mm <sup>2</sup> )	Objects			
			Bubbles	Area Pct	Particles	Area Pct
Top	9 to 12	9.06	118	1.5	25727	8.4
Middle	4 to 6	8.94	179	4.1	17143	8.1
Bottom	0 to 2	4.86	79	2.7	8301	7.2

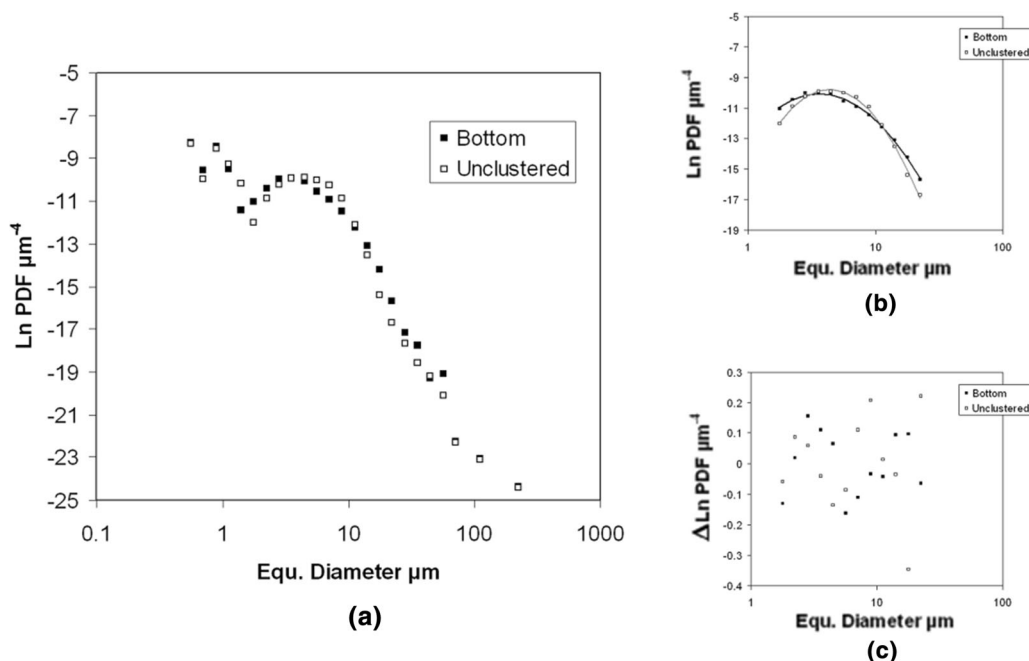


Fig. 5—Particle size distributions of alumina in inclusion rich steel zone at the impact pad, location “bottom” (see (b)). Comparison of the measurement on untreated image (black squares) against the measurement on the same image after manual separation of cluster particles (white squares). (a) The raw data (without removal of bubbles and artefacts, therefore slightly different from Figs. 6 and 7). (b) Lognormal fits for the uncorrected and unclustered data as well as residuals in Ln PDF (c).

**Table IV. Lognormal Fits to Particle Data in Figs. 5 Through 7**

Image	Fit Parameters			Peak Size (μm)
	$c_0$	$a$	$b$	
Top*	4.5E−4	1.4238	0.5299	3.14
Middle*	2.97E−4	1.4596	0.6062	2.98
Bottom*	2.45E−4	1.5426	0.5599	3.42
Unclustered <sup>†</sup>	3.1E−4	1.6571	0.4211	4.39

\*Conspicuous bubbles removed.

<sup>†</sup>Manual separation of particles on the “bottom” image.

only the easily visible open bubbles yields a bubble content between 1 and 10 vol pct for the inclusion rich zone. Thus, the zone contains roughly 90 vol pct steel and 10 vol pct combined NMI and bubble-derived voids.

### 3. NMI particle size distributions

As noted above, we employ analysis of particle size distributions of alumina in the steel clogs to investigate the formation of these inclusions (e.g., Refs. 14, 15, and 21). We have obtained particle size distributions by segmentation and object measurement on optical images at medium resolution ( $\times 200$ ). In the sample of the tundish impact zone shown in Figures 3 and 4, particle size distributions have been measured in three locations across the inclusion rich zone: bottom (contact to oxidic layers), middle, and top (contact to the main bulk steel of the tundish skull) as indicated in Figure 4; basic observational data are in Table III. The objects obtained by segmentation are in many cases not individual particles but clusters. This particle clustering (aggregation) by itself might create a change in the observed apparent size distribution compared to individual particles. To explore the effect of the particle clustering on observable PDFs, we have tried to remove



this effect on a single image (the bottom zone of the impact pad sample, shown in Figure 4), by manually separating distinguishable individual particles of the clusters. This process is by necessity subjective, and we applied the separation conservatively restricting it to only unambiguously separate appearing particles, to avoid uncontrolled overcompensation. We thus regard

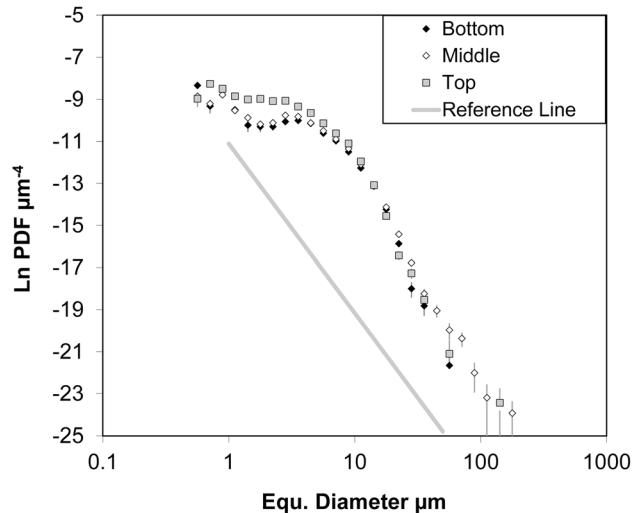
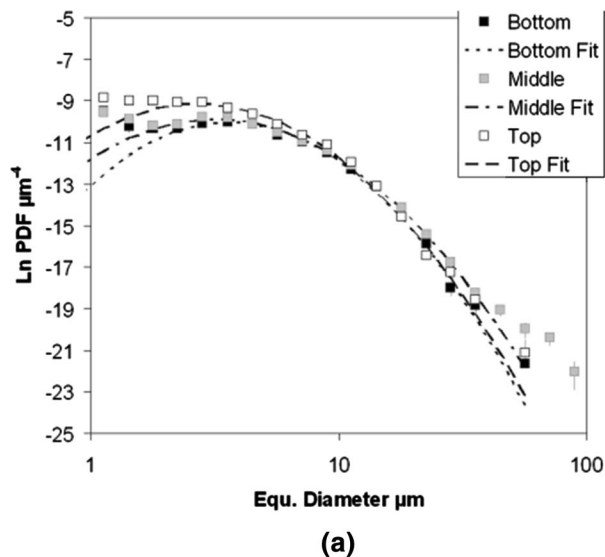


Fig. 6—Particle size distributions measured in the clogging-like inclusion rich zone at a tundish impact pad, sample shown in (a). Bottom, Middle, Top refer to three locations in a profile across the inclusion rich steel where particle sizes have been measured by optical image analysis (Figs. 5(b), (c), and (d)). Plotted are the population density functions of the underlying 3D size distributions after stereological conversion from 2D to 3D. “Reference line” is the typical power-law size distribution of alumina NMI in Ti-alloyed Al-killed steel (from Ref. [14]).



this “unclustering” as only a partial separation, showing the direction, but not necessarily the full extent of change on the PDF. As an example, the manual unclustering of the bottom area in Figure 4(b) increased the object number from 8396 to 11057. The resulting PDFs of both the original and corrected data are shown in Figure 5. As can be seen, the primary feature of both measurements is that the observed particle size distribution function is a lognormal in the size range between  $\sim 1$  and  $\sim 20 \mu\text{m}$ . At sizes below  $1.5 \mu\text{m}$ , the data are limited by imperfect optical resolution. At sizes above 20 to  $30 \mu\text{m}$ , it can be seen that the distribution changes from the curved lognormal form into a linear form albeit with significant scatter. Within these limits, Figure 5 shows the effect that the agglomeration of particles has on the PDF. As can be seen, the size distribution of the particles before agglomeration is a narrower, sharper lognormal. The effect of the combination of particles into sintered aggregates is to widen up the observed lognormal, de facto an incipient linearization of the distribution (similar to what happens to floating inclusions in the liquid steel after deoxidation). However, the quality of fit by a lognormal is not worse for the clustered cross section data; the residuals are scattered about  $\pm 0.2 \text{ Ln}$  units for both. The net effect of the clustering on the retrieved lognormal fit parameters is a decrease of the “sharpness” parameter  $b$  from 0.56 to 0.42 while the mean size parameter  $a$  increases from 1.543 to 1.657 (frequency peak size increases from  $3.5$  to  $4.5 \mu\text{m}$ ). Because of the time consuming labor involved in manual correction, we performed the unclustering only for this data set. It should be kept in mind that the clustering effect influences all the PDFs used later in this work for which no unclustering has been performed.

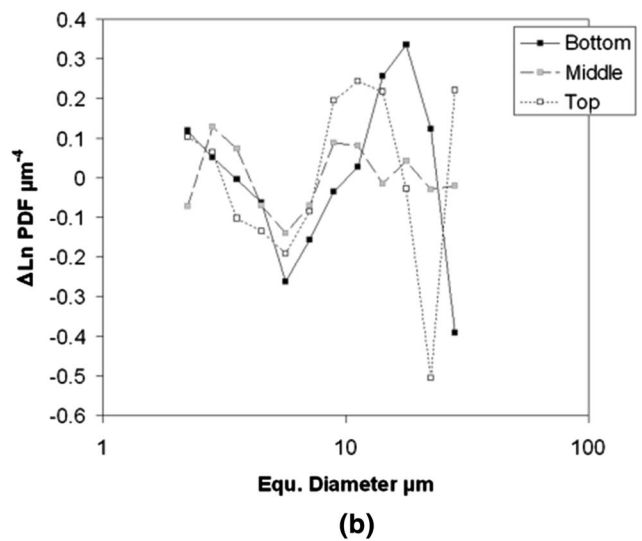


Fig. 7—Lognormal fits to the particle cluster section size distributions observed at the tundish impact pad (see Fig. 6). The lognormals have been fitted using a least squared error routine for the data range from  $2.82$  to  $22.4 \mu\text{m}$ . Fit parameters are given in Table IV. (a) The fits compared to the actual data, (b) the residuals ( $\Delta \text{LnPDF}$ ).

Table V. Spot Compositional Data for Fig. 8

Oxide	MgO	Al <sub>2</sub> O <sub>3</sub>	SiO <sub>2</sub>	ZrO <sub>2</sub>	CaO	TiO <sub>2</sub> *	V <sub>2</sub> O <sub>5</sub>	Cr <sub>2</sub> O <sub>3</sub>	MnO*	FeO*	Phase ID
Image (a)											
1	8.5	57.5	0	0	0	2.4	0.4	1.0	24.7	5.0	spinel
2	0.2	95.7	0	0	0	2.0	0.6	0	0	1.5	alumina
3	0.1	98.4	0	0	0	0	0	0	0	1.4	alumina
4	0.9	26.1	0.5	1.5	0	63.4	1.1	0.2	1.9	4.3	(Ti,Al) <sub>2</sub> O <sub>3</sub>
Image (b)											
1	27.6	68.9	0	0	0	1.3	0	0	0.7	1.9	spinel
2	47.9	2.7	38.7	0	2.3	0.2	0	0	2.6	5.2	olivine
3	0.2	1.6	0	0.2	40.0	57.1	0.5	0	0	0.3	perovskite
Image (c)											
1	0.1	77.3	0	0	21.0	0.3	0	0	0	0.3	CA2
2	26.3	69.6	0	0.3	0.2	0.2	0	0	0.9	2.0	spinel
3	2.2	83.8	0	1.0	8.1	3.8	0	0	0	0.4	CA6
4	0.3	35.6	23.5	0	38.7	0.5	0	0	0.3	0.4	gehlenite
5	0	2.3	0	0.5	39.9	55.7	0.7	0	0.2	0.6	perovskite
Image (d)											
1	0	95.7	0	0	0	0.6	0.1	0.6	0	1.5	alumina
2	0.1	54.9	0	0	0	2.2	0.3	0.5	3.0	39.2	hercynite
3	0.2	0.2	0.2	0.2	0	51.2	0.5	0	5.1	42.4	ilmenite

\*Oxide quantified in this form irrespective of true valency.

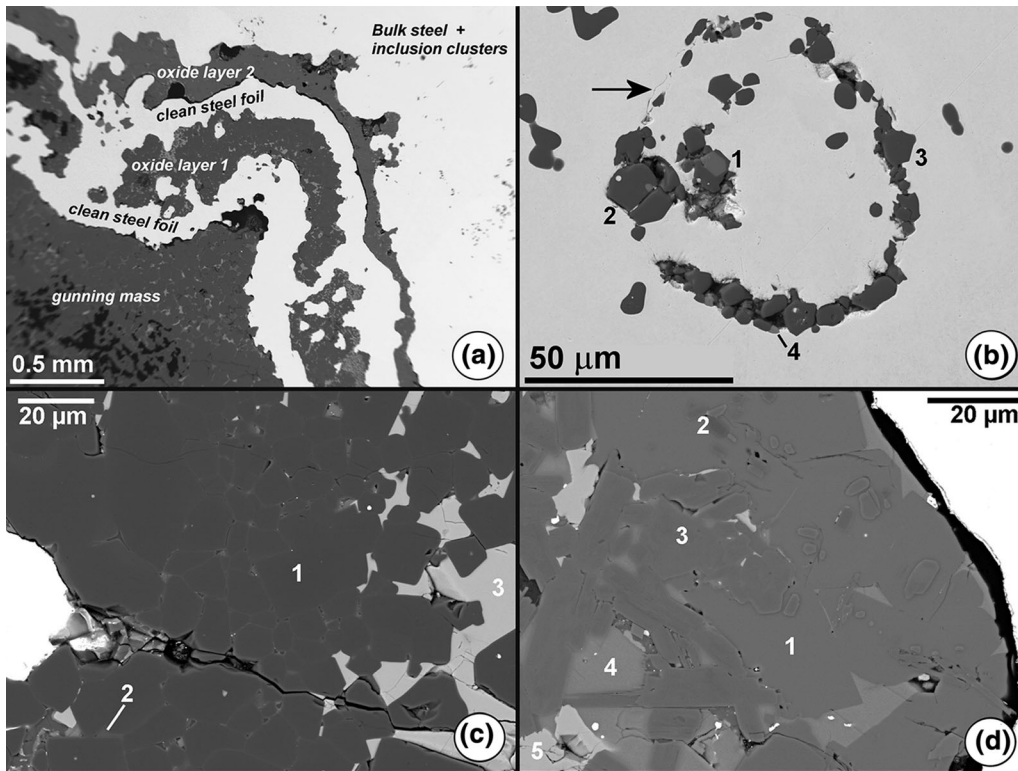


Fig. 8—Critical microstructures in the sample of the tundish bottom mid-length, shown in Fig. 2(b). All images are SEM BSE images. (a) Is a medium magnification view of the upper corner of the steel filled wedge and (e) a view of the deeper part of the same wedge. Images (b), (c), and (d) are respectively a relict inclusion encrusted bubble in the bulk steel, and views of the oxidic bands 1 and 2, respectively. The numbers in the images refer to SEM EDS analysis spots given in Table V; see there for phase identification. Arrow in image (b) points to preserved meniscus trace of the original microbubble.

A comparison of the raw clustered particle size distributions at the impact zone location is shown in Figure 6. This comparison also includes the reference line typical for NMI size distributions found in

Ti-alloyed Al-killed steel (see above). In contrast to this reference line the clustered particles in the inclusion rich steel follow a strongly curved lognormal distribution. At large sizes, above ca. 20 to 30 μm, most of the objects

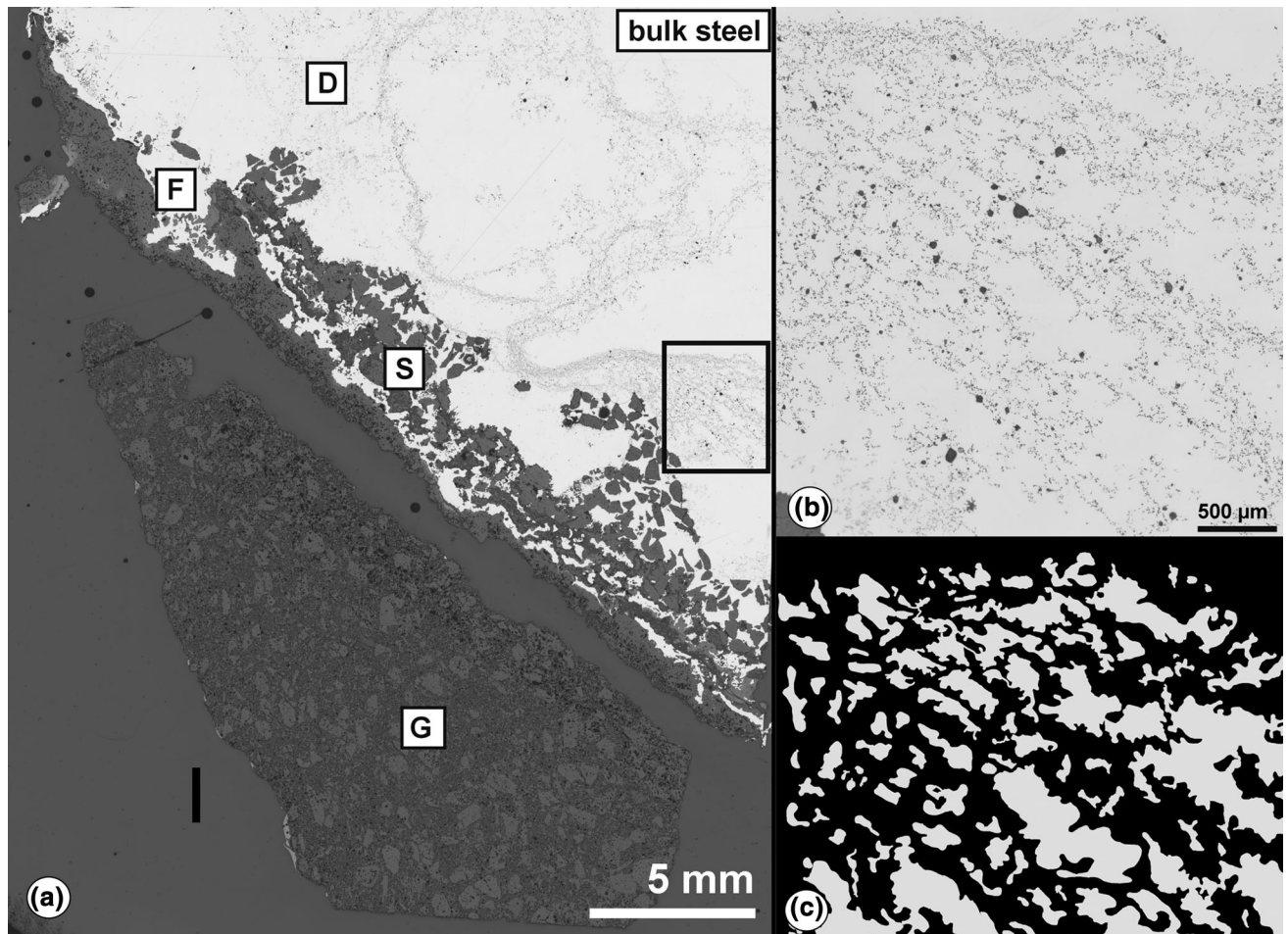


Fig. 9—Microstructures of a sample from the tundish well inlet bottom (see Fig. 2(c), and explanations there). Black box in the overview image (a) is magnified in panel (b) showing fan-like arrangement of inclusion rich lines. Panel (c) is a redrawing of this structure emphasizing inclusion free steel bodies in white, suggested to be solid delta ferrites.

appear to be fragmented remains of bubble surface encrustations, not aggregated clusters embedded in steel. This change roughly coincides with the point in Figure 6 where the size distribution begins to deviate from the lognormal shape. Table IV summarizes the fit parameters for the lognormal fits to the data, which have been based on the size range 2.2 to 28  $\mu\text{m}$  (see Figure 7). It can be observed that the fits indicate a systematic change in distribution (aggregated particles morphology) from bottom to top of the inclusion rich zone, with the topmost zone in contact to free bulk steel having the relatively smallest particles (and smallest overall deviations from a lognormal). This apparently systematic trend in NMI morphology may represent either a time-dependent trend in particle input, or a gradient in residence time and sintering (Ostwald ripening).

### B. Summary

The observations on steel skull samples at the tundish impact pad have shown that here as well sidewall materials form that resemble clogging materials like in the more operationally sensitive downstream locations. Notably, a zone of steel rich in NMI (>10 vol pct) is

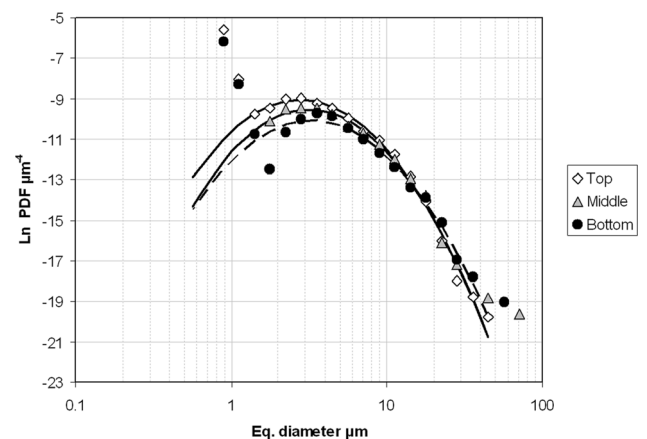


Fig. 10—Size distributions of clustered alumina particles in the highlighted depositional structure in the tundish well clogging sample shown in Fig. 9. Distributions are shown as population density functions. Top, middle, bottom refer to inclusion concentration lines in the respective parts of the structure. The drawn lines are lognormal model fits to the data based on the size range 2.82 to 22.4  $\mu\text{m}$ . Dashed line is fit to the Bottom data, solid lines are for middle and top, respectively.



**Table VI. Lognormal Fits to Particle Data in Fig. 10**

Layer	Fit Parameters			Peak Size ( $\mu\text{m}$ )
	$c_0$	$a$	$b$	
Top	5.6E-4	1.3513	0.5738	2.78
Middle	3.8E-4	1.4669	0.5584	3.17
Bottom	2.49E-4	1.5417	0.5952	3.42

found here that resembles tundish clogging material as described in the literature and in our other samples (see below). This inclusion rich zone, which can loosely be called a clogging deposit, consists of three main microstructural elements: (1) oxide particles, overwhelmingly alumina of 1 to 10  $\mu\text{m}$  size, which are more or less sintered and aggregated into small clusters, or else captured on the surface of abundant microbubbles; (2) The microbubbles in the size range of 10 to 100 seconds of  $\mu\text{m}$  which typically have particle-encrusted surfaces, and appear in variable stages of bubble infilling with steel; (3) conspicuous inclusion free steel areas which behave like “steel particles”, with sizes in excess of 100  $\mu\text{m}$  and which we interpret as relicts of delta ferrite crystals from partial solidification during casting. The material formed from these elements does not rest directly upon underlying refractory substrate (gunning mass) but is separated from this by inclusion free steel foils (likely never remelted freeze-on steel) as well as distinct layers of compositionally variable oxidic/slag-like materials that can not be derived from a steel-gunning mass reaction and therefore must be depositions out of the passing steel stream. A detailed morphological analysis of the NMI particles in the inclusion rich zone shows that they have lognormal size distributions, in strong contrast to the known power-law distributions of NMI floating in the liquid bulk steel. The deviant size distribution is not caused by local clustering, as clustering has the opposite effect (incipient linearization, which we observe in our data). The ensemble of NMI clusters, inclusion free steel bodies and microbubbles has the characteristics of a sidewall partial solidification zone, “mushy zone”, in which the clustering NMI particles are entrapped, while the steel itself (delta ferrite) is the main sediment. The chemical heterogeneity of the NMI is incompatible with reoxidation growth of the alumina in situ in the mushy zone. Their lognormal particle size distribution suggests that they have grown in an environment separate from the bulk steel, where they were not affected by the linearization that affects the bulk liquid steel floating inclusions.

### C. Steel gunning mass interface at plain tundish bottom

The steel-refractory interaction was studied halfway through the length of the tundish. An exemplary polished mount containing the steel-refractory interface at this location is shown in Figure 2(b). A feature of the steel-refractory interface at the tundish bottom is a network of cracks in the gunning mass, from drying before casting. These cracks are infiltrated by liquid steel

as the tundish is filled for the first time. Figure 2(b) contains a cross section of such a steel filled crack. Next to the crack, along the tundish bottom a sequence of thin layers of inclusion free steel can be observed, which are interlayered with thin bands of oxidic, partially solidified slag-like materials. Figure 10 shows details of this sequence, where two oxidic bands are stacked, each 0.2 to 0.3 mm thick and separated from the gunning mass and each other by similar 0.2 to 0.3 mm thick steel layers that do not contain any NMI. Phase compositional data by SEM EDS are given in Table V. They show that both bands are different in their phase makeup: the lower band consists of MA (spinel) crystals with some interstitial CT (perovskite) and trace M2S (forsterite). In the upper band an old generation of MA + CA6 is replaced by CA2 + C2AS (melilite) while CT persists. Thus, both oxidic bands reflect very different chemical environments (Ca poor versus Si poor) and both are incompatible with a derivation from the underlying gunning mass (which is a forsterite-periclase mix), even though the whole sequence of layers is only between 1 and 2 mm thick. The oxidic layers have maintained coherence and mutual separation. If the steel surrounding them had been liquid during casting, the layers could not preserve their observed shapes: they would have to coalesce into minimum surface energy forms (droplets) or even float outright. Their morphological and compositional persistence as distinct units therefore means that the steel between the oxide layers was essentially solid during the cast. We interpret them as freeze-on steel from an early time of the cast (first heats). Consequently, the oxide bands are material that was transported by the steel flow to the location where they became draped over solidified steel along the refractory contact. The material source of the observed oxide layers during casting was upstream, most likely in the ladle. Any remelting of the steel would have immediately destroyed the chemical and physical separation of these oxide marker bands, implying that the freeze-on steel never remelted during casting. Solid state of the steel must also be assumed for the steel in the infiltrated gunning mass crack, since this steel extends finger-like into a cool environment. The bulk steel (zone D, above both complex layers and steel filled crack in the tundish bottom) is rich in loose fragments of clustered alumina as well as microbubbles. An example of such a microbubble is shown in Figure 8(a); this bubble was infilled with steel but is recognizable by the ring-like encrustation of NMI collected on its former surface. The individual NMI making up the bubble encrustation ring have very disparate origins: alumina with  $\sim 2$  wt pct  $\text{TiO}_2$  occurs next to wholly Ti-free alumina, highly Ti enriched  $(\text{Ti,Al})_2\text{O}_3$  particles, as well as even Mn-rich spinel (encapsulated in alumina). All these particles can not be in chemical equilibrium with each other and most not with the surrounding steel, yet all are collected on the bubble and have survived entrapment, residence and cooling within the steel. However, the spectrum of particles observed in this bubble ring and in other cluster fragments at this sample location is consistent with the alumina and oxide

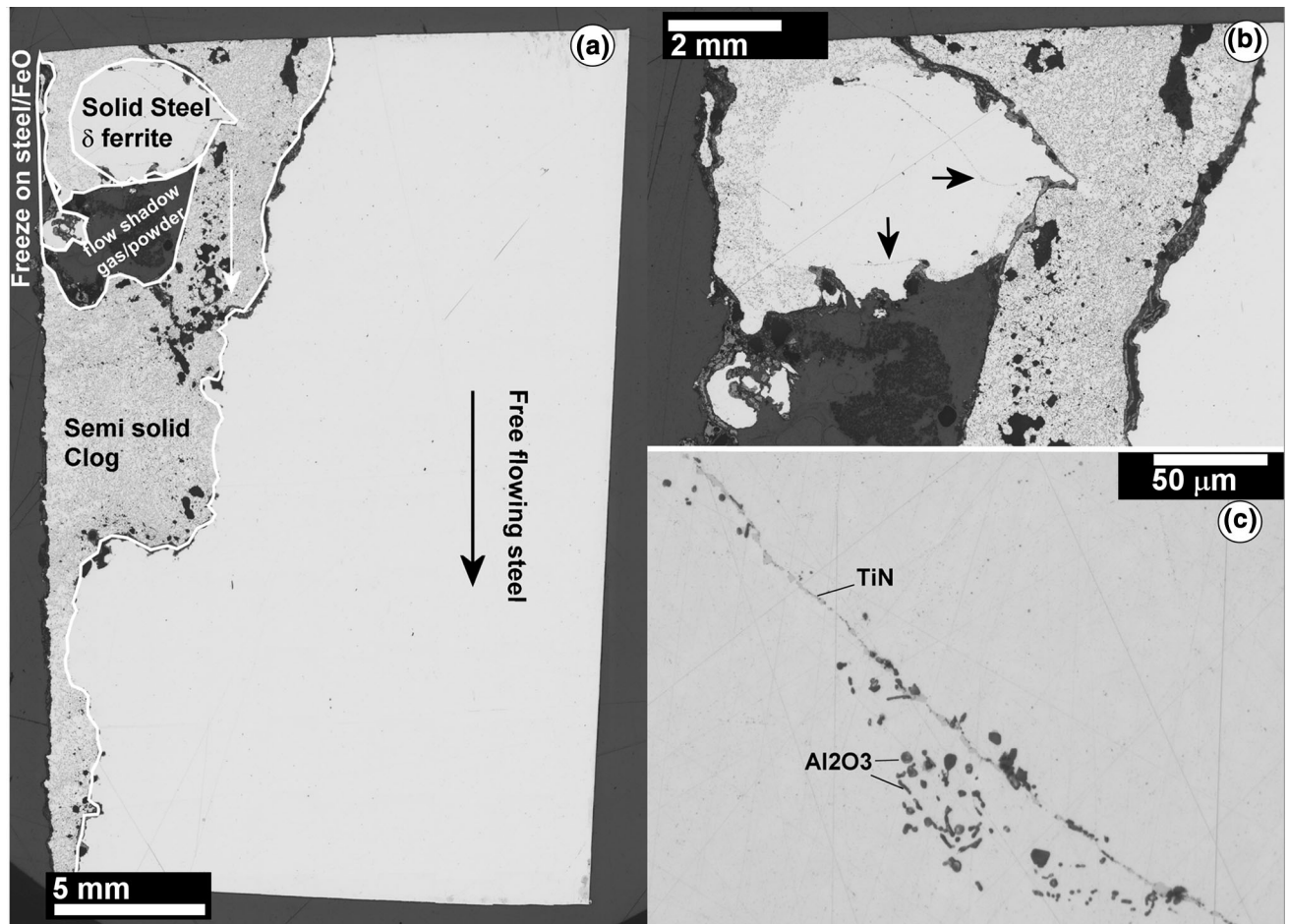


Fig. 11—Overview reflected light image of the tundish nozzle wall sample (see Fig. 2(e)). (a) Kinematic interpretation of the microstructure. Black arrow indicates flow direction of steel towards the sliding gate; white arrow indicates a bubble “trail” in flow direction downwards from the nose of the delta ferrite phenocryst. (b) Enlargement of the steel body (delta ferrite) embedded in the clogging deposit, arrows point to TiN lines. (c) Enlargement of one of the TiN lines, TiN is mid gray,  $\text{Al}_2\text{O}_3$  clustered inclusions are dark gray.

microstructures observed under the ladle shroud (impact zone) described above. This suggests that a bottom stream of liquid steel exists flowing from impact zone towards the tundish outlets which is loaded with microbubbles and fragments of clustered alumina and other oxides.

#### D. Summary

The observations on the tundish bottom midway between ladle shroud and tundish well establish that the steel solidus isotherm can reside inside the steel skull not only on cast initiation but, at least over a part of the tundish bottom surface, for the entirety of the casting duration. This implies that a “mushy zone” of partially solidified steel should exist here during normal casting operations, which may shrink or grow due to temperature gradient variations in response to the overall temperature of the bulk steel. Microstructures above the freeze-on layers suggest that a transport towards the tundish wells of fragments and preformed clusters of alumina and other oxides happens in this boundary layer.

#### E. Zone: Steel Gunning Mass Interface in Tundish Well

The tundish well inlet is the region where the tundish floor, covered by gunning mass, curves down to the tundish nozzle itself (see sketch in Figure 1, zones a, b). This is the zone where those clogging deposits form that are most characteristic for Ti-alloyed steels in contrast to non-Ti alloyed Al-killed steels, the classical inclusion rich steel zones. They develop gradually from the flat tundish floor, where inclusion concentrations build-up in distinct patches or inclusion concentration planes (zone a) before assembling into massive inclusion rich zones (zone b) with a marked interior microstructure with variations in clustered inclusion density, bodies of inclusion free steel, microbubbles, and an overall morphology shaped by flowing steel liquid. As representative examples of microstructures in this region, two sample overviews are shown in Figure 2. One of these is shown in more detail in Figure 9, together with an enlargement of a typical microstructure for this region. In this structure, which rests upon the remains of well filler sand used in this cast, inclusion enriched lines fan out downwards (in flow direction) reminiscent of

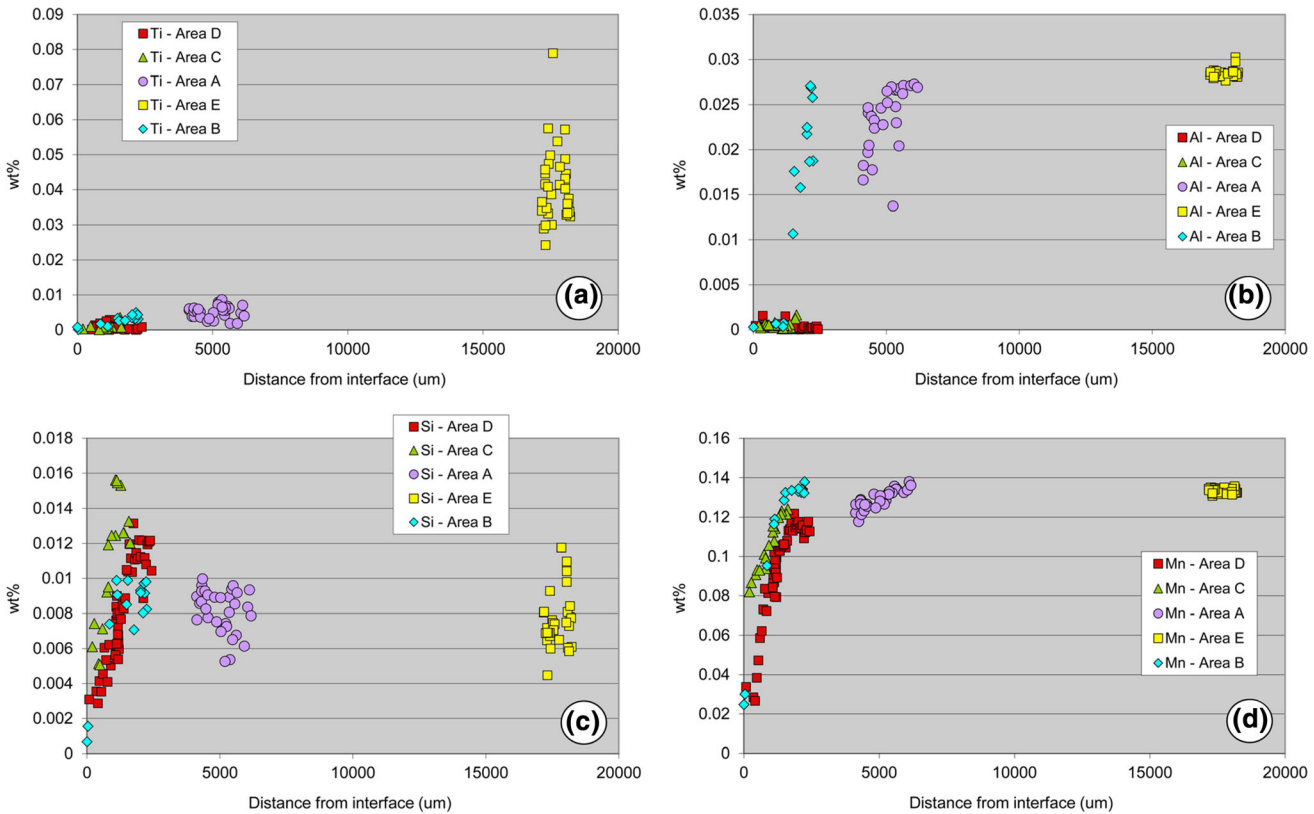


Fig. 12—EPMA minor element data, as covariation versus distance from the gunning mass contact. (a) Ti, (b) shows Al, (c) Si, and (d) Mn in the steel as a function of distance of the respective analysis spots from gunning mass contact.

sediment beds in a sand dune. They are separated by inclusion free steel areas (as drawn in Figure 9), and the whole structure is rich in microbubbles, all of which attach to the inclusion concentration lines and avoid the inclusion free steel areas. The structure is interpreted as a sedimentary (dune-like) pile-up, but not a sedimentation of clustered alumina aggregates per se, as this would not explain the inclusion free steel bodies. Instead, these steel bodies are themselves interpreted to be delta ferrite crystals grown already during casting. The dune-like arrangement is primarily caused by the sedimentation of these delta ferrites, with inclusion clusters (and microbubbles) trapped in liquid steel between the delta ferrites. It should be noted that the microstructure changes gradually towards the top of the deposition pile and the top layer presents a densely populated inclusion concentration line, adjoining to an extension of the main homogeneous bulk steel of the cast. This inclusion concentration line thus likely marks the stationary surface between fully molten steel and a pile of deposited solidified steel grains, bubbles, and interspersed clustered alumina aggregates.

If the structure pictured in Figure 9 represents a coherent depositional unit, then its base to top profile should represent an age progression, with the clustered alumina aggregates at its base having been “deposited” earlier, and having a longer time to undergo morphological sintering in place. To test whether a

morphological change is measurable across such a single depositional unit, we have performed clustered alumina size distribution analysis based on optical segmentation of the image region highlighted in Figure 9, employing the same methods as described above for Figures 6 and 7. At the bottom, in the middle and in the top of the structure, an inclusion concentration band was segmented, yielding ~ 3000, 1500 and 7800 segmented objects respectively in areas of 0.6, 0.3 and 1.1 mm<sup>2</sup>, respectively. We found the local particle concentrations in the inclusion concentration lines to be 9.7, 11.3 and 11.3 vol pct, respectively, indicating no substantial variation in inclusion amount within an inclusion concentration band. The size distributions of the bottom, middle and top layers of the structure are shown as population density function plots in Figure 10. In this figure, the clustered alumina particles display very similar size distributions of generally lognormal form between 1 and 30 μm, like in the tundish impact pad area. Fit parameters are given in Table VI. The microbubbles create the straight-line turn-off from the lognormal shape at sizes > 30 μm, and subsolidus precipitate formation in the steel after solidification causes the sudden increase in particle population densities below 1 to 1.5 μm. Regarding the alumina particle distributions, the large-size limb of the distributions can be very well modeled as a lognormal, whereas the low size limb (below peak frequency) tends to decline steeper



than a symmetric lognormal. This is most apparent for the bottom-layer data, where the skewness is unmistakable in Figure 10. The skewness diminishes towards the top layer, where the distribution is nearly symmetric about the peak. Thus there is a systematic morphological change of the alumina inclusions in the depositional unit, with a pronounced lack of smaller particles in the bottom layer. This lack of small particles increases with depth in the analyzed clogging microstructure, thus it increases with residence time of the clustered alumina at this location. This morphological behavior (selective loss of fines and insignificant change of large inclusions; decreasing variance at gradually increasing mean size) is the signature behavior of in situ Ostwald ripening of a particle population.<sup>[24,25]</sup> We take this as evidence that the interpretation of the observed clog microstructure as a depositional fan (dune) is correct. There is an age progression from bottom to top, where deposited clustered alumina at the bottom had enough time to measurably coarsen.

For such Ostwald ripening to operate, efficient mass transfer of  $\text{Al}_2\text{O}_3$  must be possible from dissolving small particles to growing large particles. Trapping of alumina inclusions in the interdendritic liquid steel between the accumulated solidified delta ferrites is consistent with this requirement. Direct evidence that the depositional fan described here indeed contained a significant melt fraction for an extended time comes from an analysis of TiN crystals that precipitate in the given steel composition close to but above solidus temperatures (see e. g. Scheil modeling by Ref. 26). TiN can be segmented optically from high-resolution images based on its distinctive color. We found an overall volume fraction of TiN of 0.3 vol% across the analyzed microstructure. This represents a local bulk content (including the delta ferrite bodies) of roughly 51 ppm N bound in TiN, which is significantly higher than the cast bulk steel (ca. 20 ppm) and suggests melt percolation and capture of nitrogen between the packed delta ferrites to support the TiN growth.

#### F. Zone: Steel—Refractory Interface in the Tundish Nozzle (Vertical Section)

As shown in Figure 1, the liquid steel exits the tundish through the vertical tundish nozzle stone, which is a porous alumina-mullite based shaped ceramic, through which Ar is injected into the flowing steel. In the tundish under investigation, steel flow is regulated by sliding gate, so that the steel-refractory interface inside the upper nozzle remains undisturbed on shutdown of casting and can be easily sampled after cooling and dropping of the tundish skull. The microstructures in the sample from this location which is shown in Figure 2 are taken here as exemplary, and an enlarged view is shown in Figure 11. The contact between refractory and nozzle bore is lined by an extensive layer of clogging deposit, consisting of steel rich in oxide inclusions, overwhelmingly alumina, as in upstream samples. Here, the distribution of alumina clustered particles throughout the clog is relatively uniform, large inclusion free bodies are small and infrequent or absent. In the sample shown

in Figure 11, there is one very large, rounded steel shape embedded in the upper part of the clogging deposit. This shape represents a large piece of already solid delta ferrite that was captured and built into the growing clogging deposit. This is shown by thin continuous TiN bands cementing segments of this body together (Figure 11). In accordance with the interpretation of this steel as a solid steel body incorporated into the clog, a gas filled void is present under it in flow shadow position, where Ar could accumulate. This void also contains loose alumina powder; and a trail of small gas bubbles extends downwards from the exposed tip of the steel body, further indicating that the structural arrangement formed while steel was flowing downward, during casting. The clogging deposit has an irregular outline in detail to the free steel. This outline is largely covered by a thin film of gas, likely trapped argon. The overall clog structure indicates semi-solid behavior during casting. The relative uniformity of the agglomerated alumina microstructure of this sample is typical for clogging materials we encountered within the tundish nozzle (zone c, Figure 1). The absence of conspicuous inclusion free steel bodies in the general clog microstructure at this location indicates that the mechanism of deposition of the mass of clustered alumina in steel does not require sedimentation of preformed solid steel bodies (as was the case in the sample discussed previously). Nonetheless, the absence of a structural gradient of inclusion density or inclusion shape, coupled with the abruptness of the transition from clog microstructure to inclusion free steel, implies that the structure has not formed through cluster agglomeration in situ, but rather through the arrest of a kinematically separated sidewall stream of particulate matter carrying steel (where gas bubbles, solidified steel bodies and clustered alumina together make up the particulate load).

#### G. Minor Element EPMA Data

The above descriptions of the microstructures encountered at the various parts of the tundish skull suggest that parts of the steel at the refractory contact have been solid throughout and the entire steel liquidus-solidus temperature interval may lie inside the steel, setting up a partially solidified mush zone. If such a mush zone exists, the compositional fractionation between early formed delta ferrites and early partial steel melt should apply. This is especially true for Ti which is after Mn the main alloying element in this steel and at the same time has a partition coefficient  $k = \text{Ti}(\text{solid})/\text{Ti}(\text{liquid})$  that is significantly different from 1 (variably cited as 0.2 to 0.4, see Ref. 27). Thus, Ti fractionation should develop in such a mushy zone, with Ti-depleted early delta ferrites. The further compositional development of such a mushy zone would depend strongly on whether the zone behaves as a closed volume with negligible melt exchange with the bulk steel, or whether it is continually being resupplied with fresh steel and back-feeds partial melt into the bulk steel. To check whether such compositional fractionation exists, we have performed EPMA minor element analyses of a clog sample from the tundish well. EPMA excitation volumes

in the steel are as large as inclusions, which together with the very dense inclusion spacing of the clogs and the inaccuracy of programmed EPMA stage movements restricted the analysis effort to hand-placed spot analyses instead of a coherent linescan. The distance of all spot analyses to the nearest steel-refractory contact (gunning mass) was measured and the analyses were compiled to yield a qualitative line profile of steel composition versus distance from contact. This pseudo-linescan is shown in Figure 12 for the four most important minor elements in the steel, Mn, Si, Ti and Al. All four elements are depleted at the edge of the steel, the contact to the gunning mass. From there, although the coverage is spotty, the elements all have attained their nominal bulk steel (alloyed) values at a location about 18 mm from the refractory contact, which corresponded to the top surface of the clog at this location. Mn, Ti, and Al all rise monotonously to this value, but Si goes through a clearly visible maximum at roughly 1 to 2 mm distance from the steel interface where it reaches values up to 150 ppm, significantly higher than the background Si in the as-cast steel. Of special importance is the composition in a distance of 5 to 6 mm from the steel interface. Here, Al has already reached bulk alloying level, whereas Ti is still severely depleted at  $\sim 100$  ppm. The data show the effects of different processes acting on the steel composition in the tundish clog. Depletion of all elements at the very outside edge of the steel is the signature of postoxidation with incipient scale formation. Diffusion of oxygen into complex steel leads to sequential oxidation of the alloy elements in the order of their affinity for oxygen, which often precipitate out as globular oxides. The depth of oxidative depletion of the alloy elements increases with increasing affinity for oxygen, and is therefore deeper for Al than for Ti. This sequence is not followed in Figure 12: we observe Ti to drop to low values within the clogging deposit at a much higher distance from the steel edge than Al. We can therefore rule out postoxidation as origin of the compositional variation in the depth of the clog. The maximum observed in the Si profile close to the tundish bottom is an indication for reactive exchange between steel and refractory during casting: the alloyed Al of the steel reduces some of the silicate (olivine) of the gunning mass, releasing reduced Si into the steel. This effect is well known for casters on the scale of the bulk steel composition, which measurably picks up Si during tundish passage. Thus, at 1 to 2 mm from the steel-refractory interface, the change of steel compositions due to oxidation after process is insignificant, and compositional relations in the inner clogging deposit reflect processes during the casting. Specifically, at 5 to 6 mm distance from the gunning mass, the steel between the clog inclusions has Ti contents as low as  $\sim 50$  ppm while Al ranges from 150 to 270 ppm (Figure 12). At a bulk Ti of 450 ppm for this cast, a perfect Scheil first-formed delta ferrite would be expected to have a concentration of about 180 ppm. The observed Ti depletion is significantly stronger than this. However, the real compositional evolution in a mushy zone is complex, including liquid steel exchange with the free steel reservoir, and back-diffusion between solidified

ferrites and interdendritic liquid. The data presented here are too fragmentary to allow a quantitative evaluation in a full segregation model.<sup>[26,27]</sup> Instead, we take them as qualitative evidence supporting the suggestion that the clog does contain remnants of a partially solidified zone with delta ferrites agglomerating at the tundish bottom during casting.

#### IV. DISCUSSION

As noted in the introduction, the microscale mechanisms operative in the formation of tundish clog materials in Ti-alloyed steels are not well understood, due to the impossibility of observing clogging growth mechanisms in situ and the difficulty of obtaining post-mortem materials from industrial practice. This study was designed to provide adequate post-mortem sample material, and the most important observational results are the following.

1. The direct contact of the steel body to the adjoining refractory (gunning mass, nozzle castware) is made by solidified steel, which freezes onto the contact material and at least in some locations does not re-melt even during extended casting series. This is unequivocally shown by the above described microstructures at the tundish bottom and nozzle interfaces. The entire temperature interval between steel solidus and liquidus therefore can lie inside the steel, which means that there is thermal potential for the formation of mushy zones of partial solidification along the tundish including its sensitive outlet zones.
2. We observed that the inclusion rich clogs consist of three distinct microstructural elements: clustered NMI aggregates (mostly alumina) themselves, but also microbubbles, and characteristic “inclusion free areas” of steel. These “inclusion free areas” have sizes (100 to 200  $\mu\text{m}$  in most cases) and multilobed shapes consistent with the morphology of delta ferrites in a “slurry casting” scenario (as described in Ref. 28). We interpret these features as actual delta ferrites formed in partially solidifying mushy zones at the margins of the steel during casting. Preliminary EPMA measurements of local steel bulk compositions in the clogs show compositional variation consistent with Scheil-type fractionation processes. Microstructural evidence suggests that these delta ferrites themselves are “clogging particles”, they are moved and redistributed along the steel sidewall trapping clustered alumina aggregates as well as microbubbles between them. The volumetric amount of these delta ferrites in a clog is large, exceeding 50 pct consistent with viscous decoupling of the sidewall stream from the bulk steel stream.<sup>[28]</sup> This implies that the actual clogging effect (hindrance of the steel flow) can be more due to the local accumulation of solidified steel than due to the actual concentration of alumina (which does not exceed a value of  $\sim 12$  to 13 vol pct in any case we studied). Further, it suggests that the often theoretically assumed “refractory attachment” mechanism (*e.g.*,

Ref. 29), based on the non-wetting of alumina by liquid steel, is irrelevant for actual clog formation. The capturing of alumina (individual particles or clusters) into the clogs involves only the gas/steel and solid steel/liquid steel interfaces, no refractory surface. However, besides clog areas with microstructures of a mushy zone we also encountered inclusion rich zones / clogs in which the clustered alumina inclusions are so homogeneously distributed that delta ferrites cannot be recognized from microstructure. These microstructural areas may represent clog areas in which the overall clog growth process is dominated more by alumina cluster capture than by assembly of already solid delta ferrites.

3. One of the most controversial issues in research on the formation of the type of clogging deposits characteristic for Ti-alloyed steels is the origin of the alumina particles observed in the clogs, and the detailed mechanism of their clustering and concentration in clogs. As the major element composition of alumina is not informative, we used the recent development of population statistical characterizations of disseminated alumina NMI<sup>[14,19,20]</sup>, to assess the origin of the alumina particles. We find that the clustered alumina aggregates of all studied clogging deposits show lognormal size distributions in the size range of 1 to 20  $\mu\text{m}$ . This distribution type is inconsistent with the power-law sizes of free floating NMI (reference line of Ref. 14), but reminiscent of the size distributions of alumina directly after deoxidation.<sup>[14,19]</sup> The discrepancy of the particle size distributions suggests that the particles in the clogs are not simply a sample of the particles freely floating in the steel. As lognormal size distributions are well known to result from active crystal growth (Refs. 16 and 24), it could be suggested that they reflect a strictly local particle origin as a simple consequence of sidewall reoxidation. However, the composition of the clogging alumina particles, especially in its  $\text{TiO}_2$  content, is heterogeneous, ranging from negligible Ti to over 2 wt pct  $\text{TiO}_2$ . These compositionally distinct types of alumina are so thoroughly mixed that both can be found even on the surface of individual microbubbles. A given steel can not be in thermodynamical equilibrium with two different compositions of alumina, showing that at least a part if not most of the alumina grains in the clog are accumulated to their location and not in equilibrium with their local surroundings. Depositional assembly of the clog is also indicated by the vast majority of microstructures (such as Figure 9). It could be suggested that the alumina particles observed in the clogs represent a separate sidewall stream of steel loaded with preformed alumina clusters as well as the extraneous slag-like oxidic materials we observe at the base of most clogs. In such a scenario, the clustered alumina could even be a remnant of the original deoxidation clusters that survived in the heat at a steel sidewall position protecting it from linearization processes operating in the bulk steel. However, neither the particle collection mechanisms at a growing clog surface nor the morphological particle development

after incorporation in a clog are well understood. We expect that the quantitative analysis of clog alumina can bring a substantial progress in understanding the primary mechanism of alumina concentration active during clog formation.

## V. SUMMARY

Based on the above summarized microstructural observations, we suggest that the buildup of clogging in the tundish well and nozzle sections happens mostly through the development of a partially solidified, “mushy” zone in which slurry casting, analogous to Ref. 28, develops. In the casting operations we studied, steel itself and other materials carried in the steel freeze on to the sidewall and never fully remelt. In the partial solidification zone between steel solidus and liquidus temperatures, delta ferrites are formed and retained. These delta ferrites, together with gas microbubbles and growing clustered alumina aggregates, develop into a steel sidewall stream that is kinematically decoupled from the overlying steel stream due to its high internal solid fraction, and this stream accumulates along the tundish bottom. In the tundish nozzle section, focused flow disrupts the flow separated mushy layer, but solidified clogging material persists into the vertical nozzle section. Direct reoxidation of the steel by reducible oxides (e. g. in the gunning mass) happens but does not play a large role. The oxide particles found in the clog are very heterogeneous in origin and are not in chemical equilibrium with local steel compositions or each other. The clog particles further have a size distribution that deviates drastically from the size distribution of floating disseminated alumina particles in the steel, but rather resembles that of newly grown clusters in such steel (whether from original desoxidation, or reoxidation during alloying, or sidewall reactions leading to reoxidation). Likely, information about the cluster formation mechanism itself is contained in the measurable particle size distributions in the clogs. The abundant microbubbles themselves collect alumina particles and the bubble capture/bubble collapse mechanism may be a competing mechanism for alumina particle concentration. Overall, the development of the tundish clogs in this type of steel can be taken as an unplanned example of slurry casting analogous to Reference 28.

## ACKNOWLEDGMENTS

We thank Tata Steel for permission to publish. Many colleagues at Tata Steel collaborated in this work. Special thanks for their collaboration go to Frank van der Does, Corrie van Hoek, Patricia Romano Triguero, Erwin Bouwens, Henk Visser, Wouter Tiekink, Arnoud Kamperman, Bernadeta Karnasiewicz and Gert Abbel. The research also profited from discussions with colleagues outside of Tata Steel,



especially In Ho Jung, Marie Aline van Ende and Joo Hyun Park. The reviewer's efforts helped to significantly improve the manuscript.

## REFERENCES

1. Y. Gao and K. Sorimachi: *ISIJ Int.*, 1993, vol. 33, pp. 291–97.
2. K.G. Rackers and B. Thomas: *Proc. 78th Steelmaking Conf.*, Nashville, 1995, pp. 723–34.
3. T. Matsui, T. Ikemoto, K. Sawano, and I. Sawada: *Taikabutsu Overseas*, 1997, vol. 18, pp. 3–9.
4. J. Smith and K. Peaslee: *AISI/DOE Technology Roadmap Program Final Report*, Pittsburgh, 2002, p. 229.
5. M. Andersson, J. Appelberg, A. Tilliander, K. Nakajima, H. Shibata, S. Kitamura, L. Jonsson, and P. Jönsson: *ISIJ Int.*, 2006, vol. 46, pp. 814–23.
6. V. Garcia da Silva: PhD thesis, PPGEM (UFRGS), Porto Alegre, 2009, p. 98.
7. K. Janiszewski and Z. Kudlinski: *Metal 2006 Conf.*, 2006, pp. 1–9.
8. L. Zhang and B. Thomas: *XXIV. Natl. Steelmaking Symposium*, Morelia, 2003, pp. 138–83.
9. A. Alekseenko, E. Baibekova, N. Kuznetsov, B. Baldaev, A. Ziborov, D. Ponomarenko, and A. Ponomarenko: *Russ. Metall. (Metally)*, 2007, vol. 7, pp. 94–97.
10. A. Pack, S. Hoernes, M. Goebbels, R. Bross, and A. Buhr: *Eur. J. Min.*, 2005, vol. 17, pp. 483–493.
11. R. Khanna, M. Ikram Ul-Haq, Y. Wang, S. Seetharaman, and V. Sahajwalla: *Metall. Mater. Trans. B*, 2011, vol. 42B, pp. 677–84.
12. J.H. Lee, M.H. Kang, S.K. Kim, J. Kim, M.S. Kim, and Y.B. Kang: *ISIJ Int.*, 2019, vol. 59, pp. 749–758.
13. M. Burty, L. Peeters, E. Perrin, S. Münzer, P. Colucci, D. Salvadori, F. Schadow, J. Valcarcel, and J. Claes: *Rev. Metall.*, 2005, vol. 11, pp. 745–51.
14. E. Zinngrebe, C. Van Hoek, H. Visser, A. Westendorp, and I.H. Jung: *ISIJ Int.*, 2012, vol. 52, pp. 52–61.
15. M.A. Van Ende, M. Guo, E. Zinngrebe, R. Dekkers, J. Proost, B. Blanpain, and P. Wollants: *Ironmak. Steelmak.*, 2009, vol. 36, pp. 201–08.
16. A. Randolph and M. Larsen: *Theory of Particulate Processes*, 2nd ed., Academic Press, San Diego, 1988.
17. M. Higgins: *Am. Miner.*, 2000, vol. 85, pp. 1105–16.
18. M. Van Ende, M. Guo, E. Zinngrebe, B. Blanpain, and I.H. Jung: *ISIJ Int.*, 2013, vol. 53, pp. 1974–82.
19. M. Seo, J.W. Cho, K.C. Kim, and S.H. Kim: *ISIJ Int.*, 2014, vol. 54, pp. 475–81.
20. W. Yang, Y. Zhang, L.F. Zhang, H. Duan, and L. Wang: *J. Iron Steel Res. Int.*, 2015, vol. 22, pp. 1069–1077.
21. O. Adaba, P. Kaushik, R. Omalley, S. Lekakh, L. Von Richards, E. Mantel, R. Hall, and E. Ellis: *Iron Steel Technol.*, 2017, vol. 31, pp. 38–49.
22. O. Adaba: Dissertation, University of Missouri – La Rolla, Doctoral Dissertations 2801, 2019. [https://scholarsmine.mst.edu/doctoral\\_dissertations/2801](https://scholarsmine.mst.edu/doctoral_dissertations/2801).
23. L. Zhang and W. Pluschkell: *Ironmak. Steelmak.*, 2003, vol. 30, pp. 106–10.
24. D. Eberl, V. Drits, and J. Srodon: *Am. J. Sci.*, 1998, vol. 298, pp. 499–533.
25. B. McCoy: *J. Colloid Interface Sci.*, 2001, vol. 240, pp. 139–149.
26. D. Kalisz and P. Zak: *Kovove Mater.*, 2015, vol. 53, pp. 35–41.
27. Z. Ma and D. Janke: *ISIJ Int.*, 1998, vol. 38, pp. 46–52.
28. M.C. Flemings: *Metall. Trans. Ser. A*, 1991, vol. 22A, pp. 957–981.
29. D.G. Zhao, M. Gao, S.H. Wang, and Y.F. Wang: *Ironmak. Steelmak.*, 2016, vol. 44, pp. 578–594.

**Publisher's Note** Springer Nature remains neutral with regard to jurisdictional claims in published maps and institutional affiliations.